Cell Reports

High synaptic threshold for dendritic NMDA spike generation in human layer 2/3 pyramidal neurons

Graphical abstract

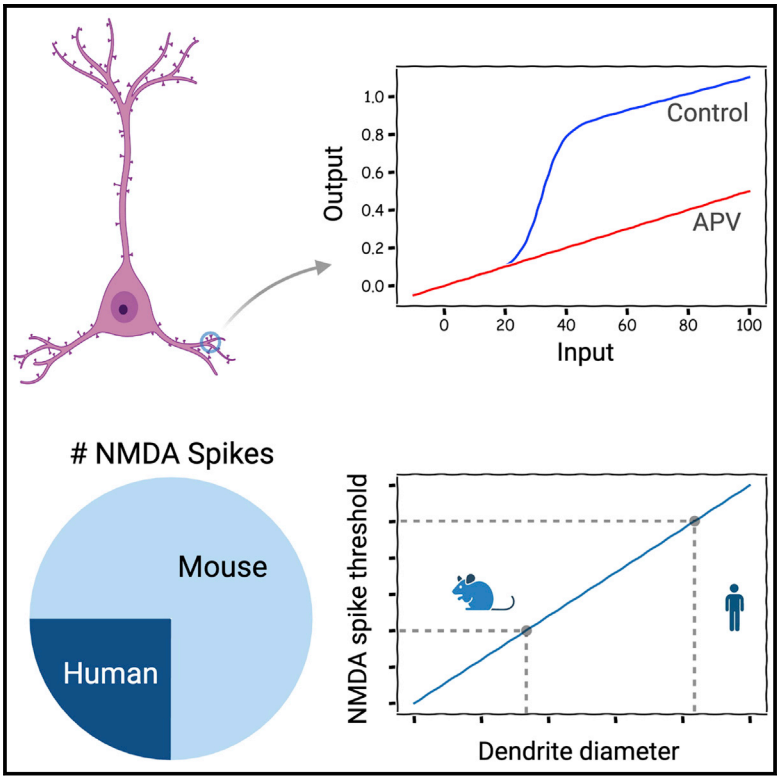

Highlights

- Human pyramidal neurons generate NMDA-receptor-dependent dendritic spikes (NMDA spikes)
- NMDA spike generation is reduced in human compared with rodent pyramidal neurons
- Differences in NMDA spike generation were reproduced in human and rodent models
- The wider diameter of human dendrites reduces NMDA spike generation in human neurons

Authors

Guilherme Testa-Silva, Marius Rosier, Suraj Honnuraiah, ..., Katharine Drummond, Lucy M. Palmer, Greg J. Stuart

Correspondence

lucy.palmer@florey.edu.au (L.M.P.), greg.stuart@anu.edu.au (G.J.S.)

In brief

Testa-Silva et al. investigate the capacity of human cortical pyramidal neurons to generate NMDA-receptor-dependent dendritic spikes and compare that with rodent neurons. They find that NMDA spike generation is reduced in human neurons and provide evidence that this is due to the wider diameter of human dendrites.

Testa-Silva et al., 2022, Cell Reports *41*, 111787
December 13, 2022
https://doi.org/10.1016/j.celrep.2022.111787

Cell Reports

CellPress
OPEN ACCESS

Report

High synaptic threshold for dendritic NMDA spike generation in human layer 2/3 pyramidal neurons

Guilherme Testa-Silva,[1,7,10] Marius Rosier,[2,3,10] Suraj Honnuraiah,[1,8,10] Robertas Guzulaitis,[2,9] Ana Morello Megias,[1] Chris French,[4,5] James King,[5] Katharine Drummond,[4,5] Lucy M. Palmer,[2,11,*] and Greg J. Stuart[1,6,11,12,*]

[1]John Curtin School of Medical Research, Australian National University, Canberra, ACT, Australia
[2]Florey Institute of Neuroscience and Mental Health, University of Melbourne, Melbourne, VIC, Australia
[3]Trinity College Institute for Neuroscience, Trinity College Dublin, Dublin, Ireland
[4]The University of Melbourne, Department of Surgery, Parkville, VIC, Australia
[5]The Royal Melbourne Hospital, Department of Neurosurgery, Parkville, VIC, Australia
[6]Department of Physiology, Monash University, Clayton, VIC, Australia
[7]Present address: Institute of Molecular and Clinical Ophthalmology, Basel, Switzerland
[8]Present address: Brain Mind Institute, École Polytechnique Fédérale de Lausanne (EPFL), Lausanne, Switzerland
[9]Present address: Life Sciences Center, Vilnius University, Vilnius, Lithuania
[10]These authors contributed equally
[11]Senior author
[12]Lead contact
*Correspondence: lucy.palmer@florey.edu.au (L.M.P.), greg.stuart@anu.edu.au (G.J.S.)
https://doi.org/10.1016/j.celrep.2022.111787

SUMMARY

Neurons receive synaptic input primarily onto their dendrites. While we know much about the electrical properties of dendrites in rodents, we have only just started to describe their properties in the human brain. Here, we investigate the capacity of human dendrites to generate NMDA-receptor-dependent spikes (NMDA spikes). Using dendritic glutamate iontophoresis, as well as local dendritic synaptic stimulation, we find that human layer 2/3 pyramidal neurons can generate dendritic NMDA spikes. The capacity to evoke NMDA spikes in human neurons, however, was significantly reduced compared with that in rodents. Simulations in morphologically realistic and simplified models indicated that human neurons have a higher synaptic threshold for NMDA spike generation primarily due to the wider diameter of their dendrites. In summary, we find reduced NMDA spike generation in human compared with rodent layer 2/3 pyramidal neurons and provide evidence that this is due to the wider diameter of human dendrites.

INTRODUCTION

Dendrites are the primary site of excitatory and inhibitory synaptic input to neurons in the brain. Understanding their properties and how they integrate information is key to understanding how the brain works. Evidence, primarily from rodents, over many decades indicates that dendrites of most neurons contain a range of voltage-activated channels that can both actively support and locally generate electrical events. A variety of active electrical events have been described in the dendrites of rodent cortical pyramidal neurons, including backpropagating action potentials (APs), as well as locally generated dendritic sodium, calcium, and NMDA-receptor-dependent spikes (NMDA spikes).[1–3] Importantly, the active dendritic properties of rodent neurons influence AP generation[1–3] as well as synaptic plasticity.[4,5] Research *in vivo* indicates that active dendritic mechanisms in rodent neurons are also critical for sensory encoding,[6–8] feature detection,[9] orientation tuning during visual stimulation,[10] correlating sensory and motor input,[11] place field formation,[12] and learning.[13]

In addition to this work in rodents, recent studies indicate that the dendrites of human cortical pyramidal neurons are also electrically excitable and can show both AP backpropagation and locally generated sodium/calcium spikes.[14–18] What is not known is whether the dendrites of human neurons also generate NMDA spikes, which are important for local synaptic integration in thin dendritic processes such as basal and apical tuft dendrites of rodent cortical pyramidal neurons.[7,19–21] NMDA spikes have also been shown to modulate AP generation as well as synaptic plasticity in cortical pyramidal neurons.[6,13,22]

Here, we investigate the capacity of human cortical pyramidal neurons to generate NMDA spikes and compare this with rodent neurons. Surprisingly, we find that the threshold for NMDA spike generation in human neurons is higher than in rodent neurons. Using simulations in morphologically realistic and simplified models, we find that this difference in excitability can be explained by the wider diameter of human dendrites. Together with our experimental findings, these simulations highlight the critical role that morphology plays in shaping the active properties of dendrites, as has been shown in previous studies in both human and rodent neurons.[15,23,24]

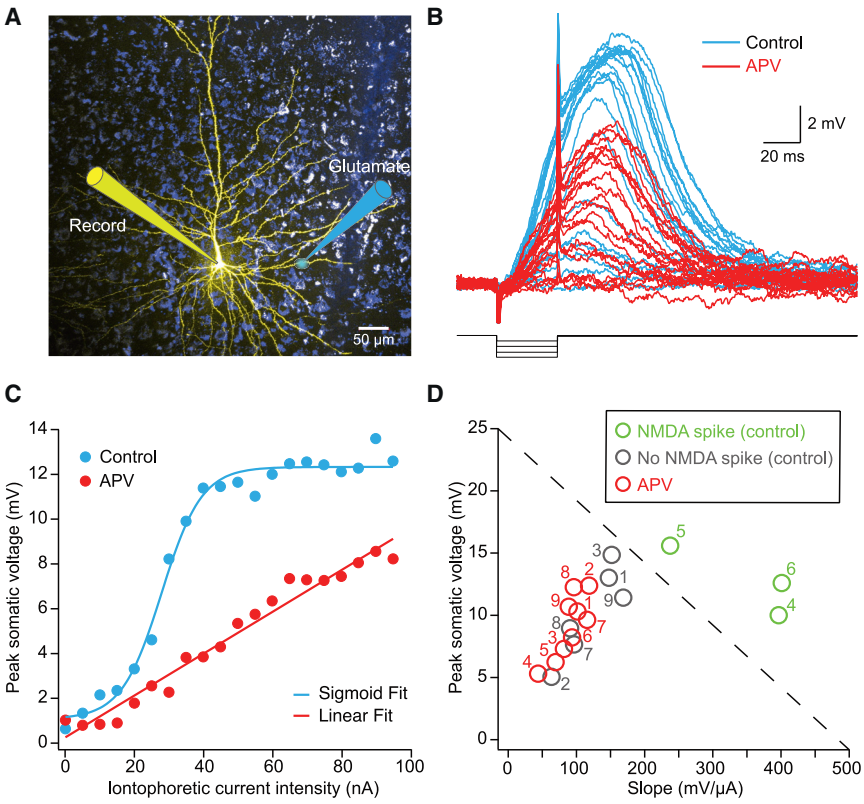

Figure 1. NMDA spike generation in human L2/3 cortical pyramidal neurons

(A) Image of a human L2/3 cortical pyramidal neuron filled with fluorescent dye via the somatic whole-cell recording pipette. The whole-cell recording pipette (yellow) and iontophoretic pipette for dendritic glutamate application (blue) are indicated schematically.

(B) Somatic voltage response during glutamate iontophoresis to a basal dendrite (~150 μm from the soma; 0 to −100 nA in 5 nA steps) in a human L2/3 cortical pyramidal neuron in control (blue) and following bath application of the NMDA antagonist APV (red; 50 μM). The timing of the iontophoretic current pulses is indicated schematically (bottom).

(C) Plot of the peak somatic voltage at the soma versus iontophoretic current intensity for a human L2/3 cortical pyramidal neuron in control (blue) and APV (50 μM, red). Same cell as shown in (B). Application of APV converted the sigmoidal voltage versus iontophoretic current relationship in control to a linear relationship. Control data fitted with a sigmoid. Data in APV are fitted with a line.

(D) Plot of the maximum somatic voltage response at the highest iontophoretic current intensity tested versus the maximum slope of the sigmoid fit in control or the slope of the linear fit in APV for human L2/3 cortical pyramidal neurons (n = 9). The dashed diagonal line represents a linear "threshold" used to differentiate cells that had a clear non-linear component under control conditions (green; indicating generation of an NMDA spike) from cells where the response was linear under control conditions (gray) and in APV (red). Individual cells before and after APV are numbered. Only 3 out of 9 (33%) human L2/3 cortical pyramidal neurons showed clear NMDA spikes during dendritic glutamate iontophoresis.

RESULTS

Whole-cell current-clamp recordings were performed from the soma of layer 2/3 (L2/3) pyramidal neurons in brains slices prepared from human tissue. We did not differentiate between L2 and L3.[25] Human brain tissue was obtained from patients undergoing neurosurgery to remove brain tumors or treat epilepsy. This tissue was either excess to that required for histopathology or was removed to allow surgical access. Written informed consent was obtained from patients (aged 19 to 71 years old), and all procedures were performed with the approval of the Human Research Ethical Committee of the Royal Melbourne Hospital. Human brain tissue was obtained primarily from the anterior medial temporal cortex and less commonly from the frontal and parieto-occipital cortex. It was macroscopically healthy and processed immediately upon removal.

Human neurons had morphology typical of cortical L2/3 pyramidal neurons and fired repetitive APs in response to depolarizing somatic current injections (Figure S1A; n = 39). Compared with rodent L2/3 pyramidal neurons, human L2/3 pyramidal neurons had lower input resistance (Figure S1B; human 35.9 ± 2.3 versus mouse 88.4 ± 2.6 MΩ; $p < 0.0001$; unpaired t test) and more depolarized resting membrane potentials (Figure S1C; human −67.7 ± 0.5 versus mouse −75.4 ± 0.9 mV; $p < 0.0001$; unpaired t test). While there was a trend for greater sag in voltage responses to hyperpolarizing somatic current injections in human compared to rodent L2/3 pyramidal neurons, as reported by others,[25] this difference was not statistically significant (Figure S1D; unpaired t test). In addition to differences in membrane potential and input resistance, we also observed a significant difference in AP height, AP half-width, and the amplitude of the AP afterhyperpolarization between human and rodent cortical L2/3 pyramidal neurons (Figures S1E–S1G; $p < 0.01$; unpaired t test). Taken together, these data indicate that from a somatic perspective, human and rodent L2/3 pyramidal neurons differ in a number of fundamental biophysical properties, suggesting they may also differ in their dendritic properties.

To investigate if human L2/3 pyramidal neurons generate dendritic NMDA spikes, we focally activated dendritic NMDA receptors using iontophoresis (Figure 1A). Briefly, a pipette containing the neurotransmitter glutamate was placed under visual control in close proximity (within a few μm) to basal and oblique dendrites (approximately 150 μm from the soma). Brief (20 or 30 ms) negative current pulses of different magnitudes were used to apply glutamate. We have previously used this method to reliably evoke NMDA spikes in the basal dendrites of rodent cortical pyramidal neurons.[26] Only cells where we could obtain iontophoretic data before and after application of the NMDA receptor blocker APV were included for analysis (n = 9 out of 21 human neurons). This technique reliably depolarized both basal and oblique dendrites (Figure 1B). Importantly, in some cases, the amplitude of somatically recorded depolarizing events

increased non-linearly with the magnitude of iontophoretic current used to apply glutamate, suggesting the generation of NMDA spikes (Figures 1B and 1C, blue). Consistent with this idea, bath application of APV (50 μM) converted this non-linear relationship into a linear relationship in some cells (Figures 1B and 1C, red). Control data were fitted with a sigmoid, whereas data in the presence of APV were fitted with a line. From these fits, we determined the maximum slope of the sigmoid in control as well as the slope of the line in APV (see STAR Methods). For each cell, we plotted the slope in control and APV versus the maximum voltage obtained at the highest iontophoretic current tested (Figure 1D). A linear "threshold" was then used to differentiate cells that had a large non-linear component under control conditions (Figure 1D, green) from cells where the response in control was similar to that in the presence of APV (Figure 1D, gray/red). The rationale was that cells with a non-linear response in control, indicative of the generation of an NMDA spike, would be expected to have a high sigmoidal slope and high maximum amplitude and so will be located in the upper right-hand quadrant. In contrast, cells where NMDA spikes were not evoked under control conditions would be expected to have reduced slope and maximum amplitude and so will be located in the bottom left-hand quadrant together with cells in APV. Based on this analysis, we concluded that 3 out of 9 human L2/3 pyramidal neurons (33%) showed NMDA spikes during dendritic glutamate iontophoresis. As evidence of the validity of this approach, application of APV lead to a significant reduction in maximum amplitude and slope in cells classified as generating NMDA spikes ($p < 0.05$), whereas there was no significant impact of APV in cells classified as not generating NMDA spikes (Figure S2; paired t test). In conclusion, these data show that human neurons can generate NMDA spikes, although this was not observed in all cells.

Since most of our current knowledge about dendritic NMDA spikes stems from work in rodent neurons during synaptic input, we directly compared the capacity of human and mouse L2/3 pyramidal neurons to generate NMDA spikes during local dendritic extracellular stimulation. As the majority of the human data were from temporal cortex, mouse recordings were also made from temporal cortex. Only cells where we could obtain extracellular stimulation data before and after application of the NMDA receptor blocker APV were included in this analysis ($n = 8$ out of 18 human neurons). In a subset of human and mouse neurons, somatic responses to local dendritic extracellular stimulation increased in a sigmoidal manner with stimulation intensity under control conditions (Figures 2A–2D, blue/black), with the relationship between extracellular stimulation strength and response amplitude linear in the presence of APV (Figures 2A–2D, red). To determine which cells had NMDA spikes, we applied the same "threshold" analysis used during iontophoretic glutamate application. This analysis differentiated human and mouse neurons with a clear non-linear component during extracellular stimulation under control conditions (Figures 2E and 2F, green), indicative of an NMDA spike, from cells where the response was essentially linear and similar to that in APV (Figures 2E and 2F, gray/red). Similar to the experiments during glutamate iontophoresis, only a small subset of human L2/3 cortical pyramidal neurons showed clear NMDA spikes during local dendritic extracellular stimulation (Figure 2E; 2 out of 8 human neurons, 25%). In contrast, the majority of mouse L2/3 cortical pyramidal neurons showed clear NMDA spikes (Figure 2F; 11 out of 15 mouse neurons, 73%). This difference in the capacity to evoke NMDA spikes in human and mouse L2/3 cortical pyramidal neurons was significant ($p < 0.05$; chi-squared test). Consistent with this finding, the impact of blocking NMDA receptors on excitatory postsynaptic potential (EPSP) peak amplitude at the highest stimulation intensity tested was significantly greater in mouse compared with human L2/3 cortical pyramidal neurons (Figures S3A and S3B; $p < 0.05$; unpaired t test). In contrast, there was no significant difference in the NMDA to AMPA component of EPSPs recorded in human and mouse neurons at the lowest stimulation intensity tested (Figures S3C and S3D). Together, these data indicate that the capacity to evoke NMDA spikes in human L2/3 cortical pyramidal neurons is considerably lower than in mouse L2/3 cortical pyramidal neurons.

To understand what underlies this difference, we simulated NMDA spike generation in morphologically realistic models of human and mouse L2/3 cortical pyramidal neurons (Figure 3A; see STAR Methods). The morphology of human and mouse L2/3 cortical pyramidal neuron models was taken from previous studies.[10,27] The intracellular resistance (R_i) and specific membrane capacitance (C_m) in the human and mouse models were set to the same value. We then varied the specific membrane resistance (R_m) in the human and rodent models so that the somatic input resistance was similar to that observed experimentally (Figure S1). To achieve this, R_m was set to 10 $k\Omega.cm^2$ in the human L2/3 pyramidal neuron model and 40 $k\Omega.cm^2$ in the mouse L2/3 pyramidal neuron model, giving somatic input resistances of 40 and 100 MΩ, respectively. As the resting membrane potential of human and mouse L2/3 pyramidal neurons is also different (Figure S1), we set the resting membrane potential of the human L2/3 pyramidal neuron model to −65 mV and the mouse L2/3 pyramidal neuron model to −75 mV. In addition to these differences, as documented by earlier work,[28] basal dendrites are significantly longer in human compared with mouse L2/3 pyramidal neurons. In addition, we found that the basal dendrites of the human L2/3 cortical pyramidal model were significantly wider than those of the mouse L2/3 model (Figure 3B; $p < 0.001$; unpaired t test).

Could these differences in electrical and morphological properties account for the reduced capacity to generate NMDA spikes in human compared with mouse neurons? To investigate this, synaptic inputs containing AMPA and NMDA components (AMPA/NMDA conductance ratio 2) were randomly distributed over a defined region (10 μm in length, ∼150 μm from the soma) of selected basal dendrites in the two models. We then activated increasing numbers of synaptic inputs until an NMDA spike was evoked in the human (Figure 3C) and mouse L2/3 cortical pyramidal neuron models (Figure 3D). These simulations were then repeated on other randomly selected basal dendrites in the two models. For each basal dendrite, the peak amplitude of the response at the soma was plotted versus the number of activated synapses and the data fitted with a sigmoidal function (Figure 3E). To determine the number of synaptic inputs required to evoke an NMDA spike, we differentiated these sigmoidal fits (Figure 3F) and defined the "threshold" number of synaptic inputs required for NMDA spike generation as the number at the

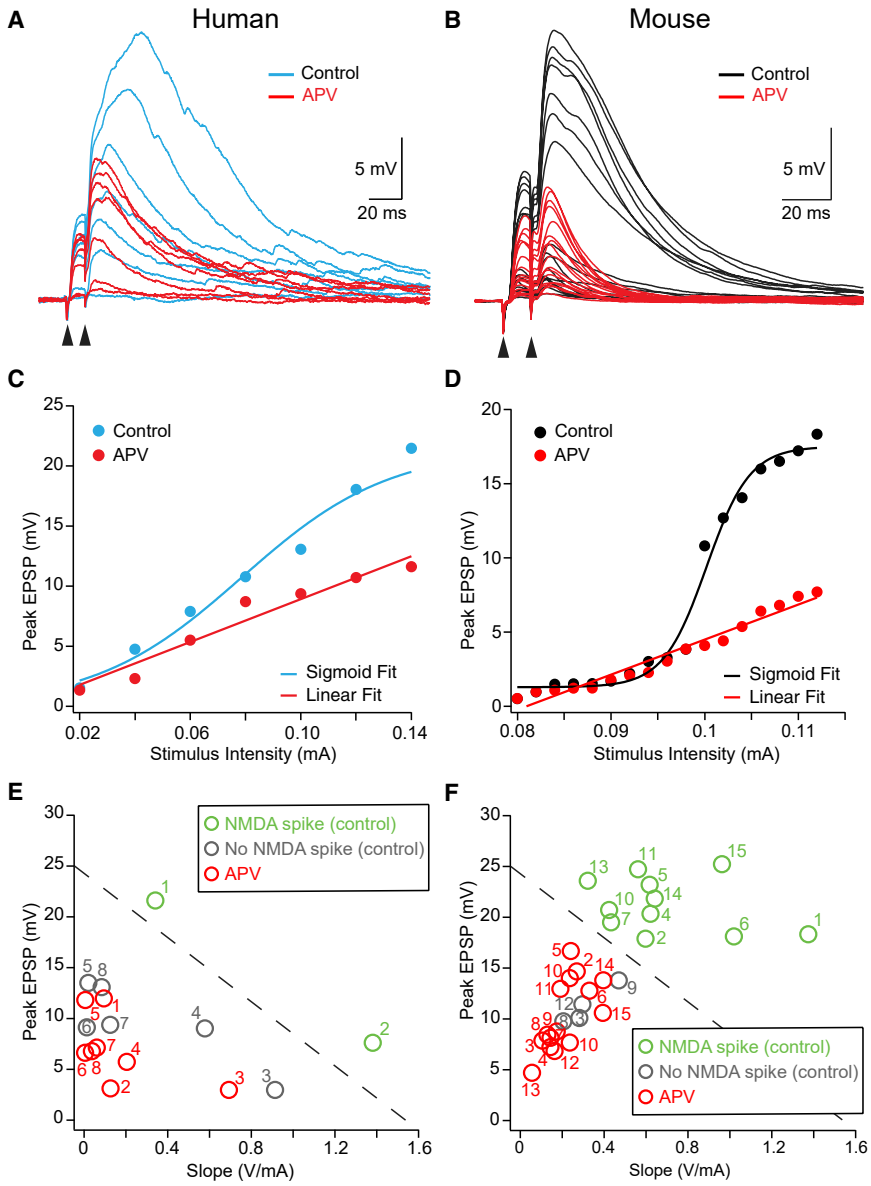

Figure 2. Comparison of NMDA spike generation in human versus mouse L2/3 cortical pyramidal neurons

(A and B) Examples of voltage responses at the soma during local extracellular stimulation (two pluses at 100 Hz; arrowheads) to basal dendrites of human (A) and mouse (B) L2/3 cortical pyramidal neurons at different intensities (human neuron: 0.02 to 0.14 mA; mouse neuron: 0.08 to 0.115 mA) in control (blue/black) and APV (50 μM, red).

(C and D) Plot of the peak somatic voltage response versus extracellular stimulation current for human (C) and mouse (D) L2/3 cortical pyramidal neurons shown in (A) and (B) in control (blue/back) and APV (50 μM, red). Application of APV converted the sigmoidal somatic voltage response versus stimulus current intensity relationship in control to a linear relationship. Control data are fitted with a sigmoid. Data in APV are fitted with a line.

(E and F) Plot of the maximum somatic voltage response at the highest extracellular stimulation intensity versus the maximum slope of the sigmoid fit in control or the slope of the linear fit in APV for human (E; n = 8) and mouse (F; n = 15) L2/3 cortical pyramidal neurons. The dashed diagonal line represents a linear "threshold" used to differentiate cells that had a clear non-linear component under control conditions (green; indicating generation of an NMDA spike) from cells where the response was linear under control conditions (gray) and in APV (red). Individual cells before and after APV are numbered. Only 2 out of 8 (25%) human L2/3 cortical pyramidal neurons showed clear NMDA spikes (E). In contrast, 11 out of 15 (73%) mouse L2/3 cortical pyramidal neurons showed NMDA spikes (F).

peak of the differentiated sigmoid, where the sigmoid slope is greatest. This analysis revealed that the number of synapses required to evoke NMDA spikes in the basal dendrites of the human model was significantly higher than in mouse model (Figure 3F). This observation was consistent across a range of basal dendrites in the two models (Figures 3E and 3F). These simulations in morphologically realistic models align with our experimental data and suggest that differences in morphology and/or the passive electrical properties of human and mouse L2/3 cortical pyramidal neurons can explain the reduced capacity of human L2/3 cortical pyramidal neurons to evoke NMDA spikes.

To investigate the impact of dendritic location on NMDA spike threshold, the location of synaptic input on a selected basal dendrite was varied from next to the soma (normalized location = 0) to the distal end of a basal dendritic branch (normalized location = 1). Consistent with earlier work,[29–31] in both the human and mouse models, the threshold synaptic conductance required for NMDA spike generation decreased when the location of synaptic input was further from the soma (Figures 4A and 4B). Importantly, NMDA spike threshold in the mouse L2/3 pyramidal neuron model was lower than in the human L2/3 pyramidal neuron model at all basal dendritic locations (Figure 4C), although this difference decreased as synaptic input was located further from the soma (Figure 4D). These simulations indicate that the lower threshold for NMDA spike generation in mouse compared with human L2/3 pyramidal neuron basal dendrites is not unique to the experimentally tested basal location (~150 μm from the soma) but is likely to apply to all basal dendritic locations in L2/3 pyramidal neurons.

Next, we used a simplified "ball and stick" model to investigate which electrical and morphological parameters underlie the difference in NMDA spike generation in the human and mouse models. This ball and stick model consisted of a somatic compartment connected to a single dendritic compartment (default dimension: 300 μm long and 1 μm wide). The default

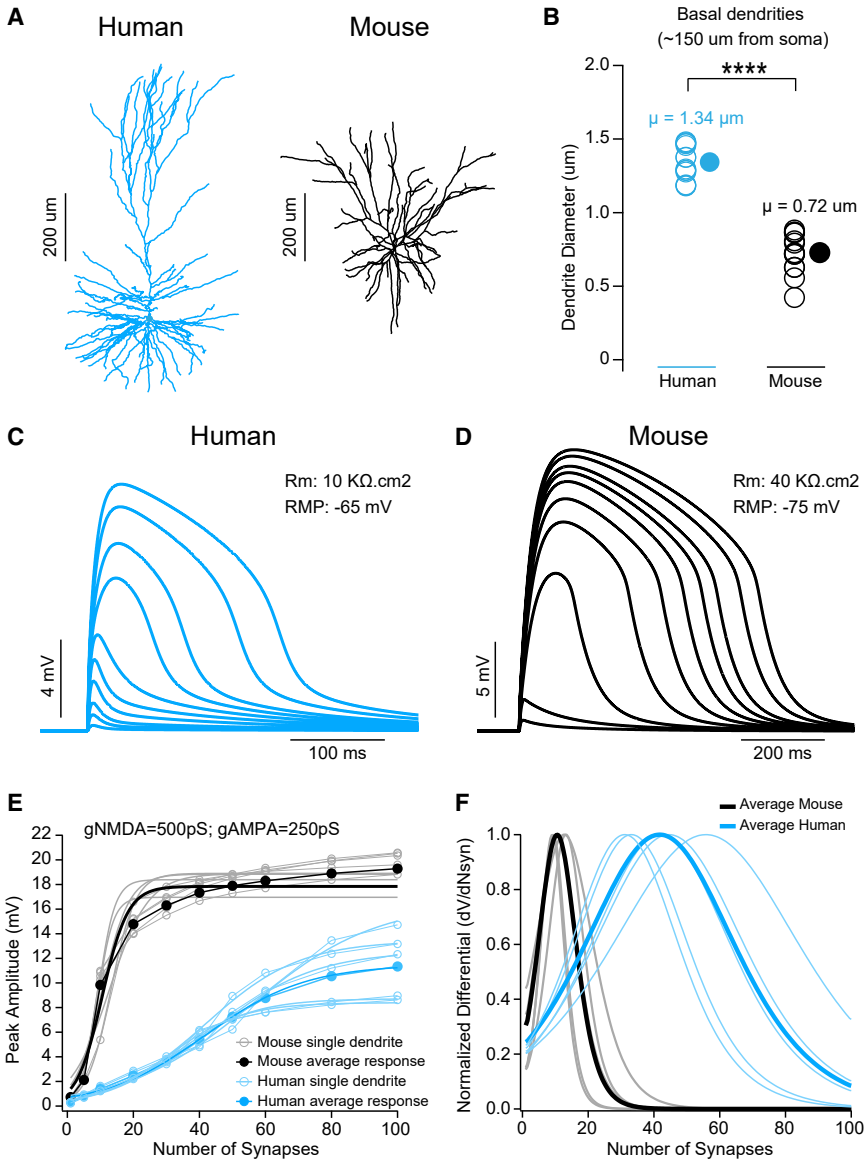

Figure 3. NMDA spike generation in morphologically realistic models of human and mouse L2/3 cortical pyramidal neurons

(A) Images of the human (left) and mouse (right) L2/3 pyramidal neuron models.

(B) Comparison of individual (open symbols) and average (filled symbol) basal dendritic diameter ~150 μm from the soma in the human and mouse L2/3 pyramidal neuron models.

(C and D) Voltage responses at the soma during activation of different numbers of synaptic inputs to basal dendrites ~150 μm from the soma in the human (C) and mouse (D) L2/3 cortical pyramidal neuron models shown in (A).

(E) Plots of the peak somatic voltage responses versus the number of activated synapses in the human (blue) and mouse (black) L2/3 cortical pyramidal neuron models shown in (A) during synaptic input onto different basal dendrites. Light lines with open symbols show responses in individual basal dendrites. Darker lines and filled symbols show the average. All data fitted with sigmoid functions.

(F) Plots of normalized, differentiated sigmoidal fits to the data shown in (E) versus the number of activated synapses in the human (blue) and mouse (black) L2/3 cortical pyramidal neuron models shown in (A) during synaptic input onto different basal dendrites. Light lines show responses in individual basal dendrites. Darker lines show the average.

passive properties were R_m = 30 kΩ.cm^2, C_m = 1 μF/cm^2, and R_i = 150 Ω.cm with a default resting membrane potential of −65 mV. A single synaptic input containing both AMPA and NMDA components was placed on the dendritic compartment 150 μm from the soma. The strength of this synaptic input was then increased by changing the magnitude of the combined NMDA/AMPA conductance (default NMDA/AMPA conductance ratio 2) to determine the threshold conductance required for NMDA spike generation. We then systematically varied the dimensions of the dendritic compartment or its passive electrical membrane properties over a physiologically relevant range to determine which parameters had the greatest impact on the threshold for NMDA spike generation. These simulations were performed in models with different dendritic diameter (Figure 5A), dendritic length (Figure 5B), R_m (Figure 5C), C_m (Figure 5D), and resting membrane potential (Figure 5E). We also tested the impact of the NMDA/AMPA conductance ratio, the extracellular magnesium concentration, and the NMDA slope factor on NMDA spike threshold (Figure S4). For each model, we fitted a sigmoid to the peak amplitude of the somatic response versus the magnitude of the synaptic conductance relationship (Figures 5A–5E, left) and then differentiated this sigmoid fit to determine the synaptic conductance at NMDA spike threshold (Figures 5A–5E, middle). Finally, we plotted the threshold synaptic conductance for NMDA spike generation versus the different electrical and morphological parameters to determine which had the greatest impact on NMDA spike generation (Figures 5A–5E, right).

These simulations indicated that differences in dendritic diameter have the greatest impact on NMDA spike threshold, with models with larger dendritic diameters having higher NMDA spike threshold (Figure 5A). Differences in dendritic length (Figure 5B), R_m (Figure 5C), C_m (Figure 5D), and resting membrane potential (Figure 5E) all had only a smaller impact on NMDA spike threshold. Differences in extracellular magnesium over the physiological range, as well as the NMDA slope factor, also had little impact on NMDA spike threshold (Figures S4A and S4B), whereas increasing the NMDA/AMPA conductance ratio decreased NMDA spike threshold (Figure S4C). While a lower NMDA/AMPA conductance ratio in human neurons could

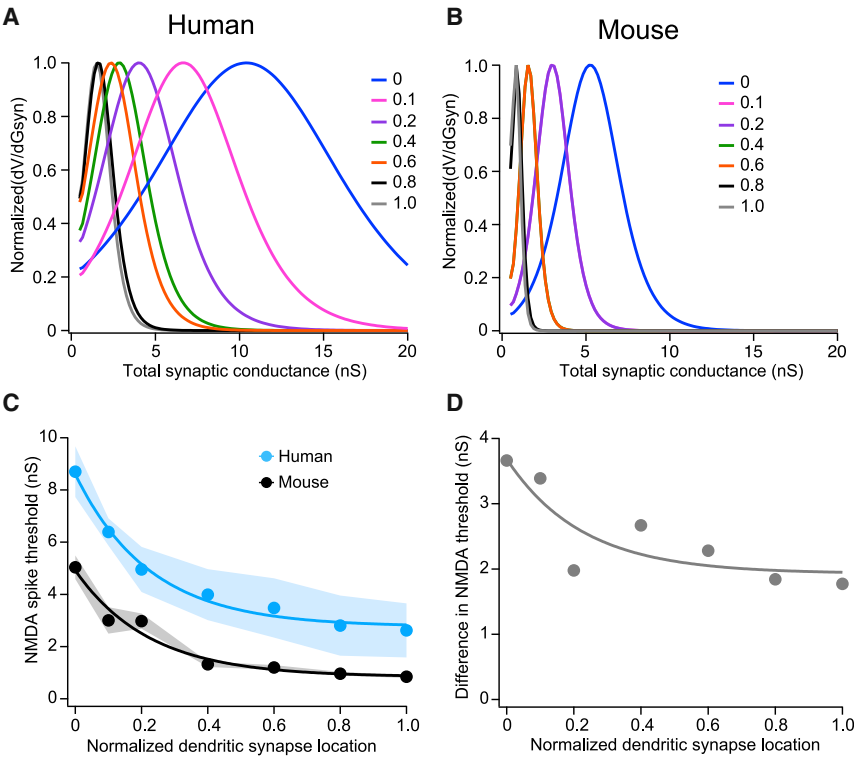

Figure 4. Dependence of NMDA spike threshold on dendritic location

(A and B) Plots of differentiated and normalized sigmoid fits to somatic responses during increases in total AMPA/NMDA synaptic conductance at different basal dendritic locations in morphologically realistic models of human (A) and mouse (B) L2/3 cortical pyramidal neurons. Data are color coded for normalized dendritic location (legend). Synaptic input located next to the soma had a normalized location of 0, whereas synaptic input at the very distal tip of a basal dendrite has a normalized location of 1.

(C) Plots of the synaptic conductance at the peak of differentiated and normalized sigmoid fits (representing the NMDA spike threshold) in the human (blue) and mouse morphologically realistic layer 2/3 models (black) versus the normalized location of synaptic input in basal dendrites. Data are averaged across multiple basal dendrites (n = 4) and fitted with an exponential function. Shading indicates standard error of the mean.

(D) Plot of the difference in NMDA spike threshold (human – mouse) versus the normalized location of synaptic input in basal dendrites. Data are fitted with an exponential function.

contribute to their higher NMDA spike threshold, this seems unlikely as we did not see a difference in the NMDA/AMPA ratio in human and mouse neurons (Figures S3C and S3D). Furthermore, recent data suggest that, if anything, human L2/3 pyramidal neurons have a higher, rather than lower, NMDA/AMPA ratio compared with mouse neurons.[32] In summary, using realistic and simplified models, we show that the reduced capacity to generate NMDA spikes in human compared with mouse L2/3 cortical pyramidal neurons is likely to be a direct result of the wider diameter of dendrites in human neurons.

DISCUSSION

Here, we show that the basal and oblique dendrites of human cortical pyramidal neurons can generate NMDA spikes, similar to previous work in rodents. These findings complement recent work indicating that, like rodent neurons, the apical dendrites of human cortical pyramidal neurons support active AP backpropagation as well as the generation of local sodium/calcium spikes.[14,15,17,18] Surprisingly, however, the ability to evoke NMDA spikes in basal and oblique dendrites of human L2/3 cortical pyramidal neurons was significantly reduced compared with mouse neurons. This finding was reproduced in morphologically realistic models, where the number of synaptic inputs required for NMDA spike generation was found to be significantly higher in human compared with mouse L2/3 pyramidal neuron models irrespective of the site of synaptic input. Using a simplified ball and stick model, we show that the synaptic threshold for NMDA spike generation is highly sensitive to differences in dendritic diameter. As the dendrites of human neurons are both longer and wider than in mouse neurons, these simulations suggest that the reduced capacity to generate NMDA spikes in human neurons is likely to be a direct result of the wider diameter of human dendrites. These findings highlight the critical role that morphology has on active dendritic properties, as has been shown previously in studies on rodent neurons.[23,24]

Our simulations indicated that the increased length of human basal dendrites may contribute to the higher synaptic threshold for NMDA spike generation in human neurons, although this effect was small (Figure 5B). In contrast, lower C_m values as well as more depolarized membrane potentials will act to decrease NMDA spike threshold, although these effects were also small (Figures 5D and 5E). A similar dependence of NMDA spike threshold on membrane potential has been observed experimentally in rodent neurons.[30] This dependence of NMDA spike threshold on membrane potential is in the opposite direction to explain the higher NMDA spike threshold in human L2/3 pyramidal neurons, which are more depolarized than mouse L2/3 pyramidal neurons (Figure S1). Our simulations also show that membrane potential and dendritic length have opposite effects on NMDA spike threshold. As a result, the impact of the more depolarized membrane potential of human L2/3 pyramidal neurons on NMDA spike threshold will be offset by the increased length of human compared with mouse basal dendrites.

The parameter that had the greatest impact on NMDA spike generation was dendritic diameter (Figure 5A). Increasing dendritic diameter from 0.75 to 1.25 μm, that is, over a range similar to the observed difference in basal dendritic diameter in the mouse and human L2/3 pyramidal neuron models

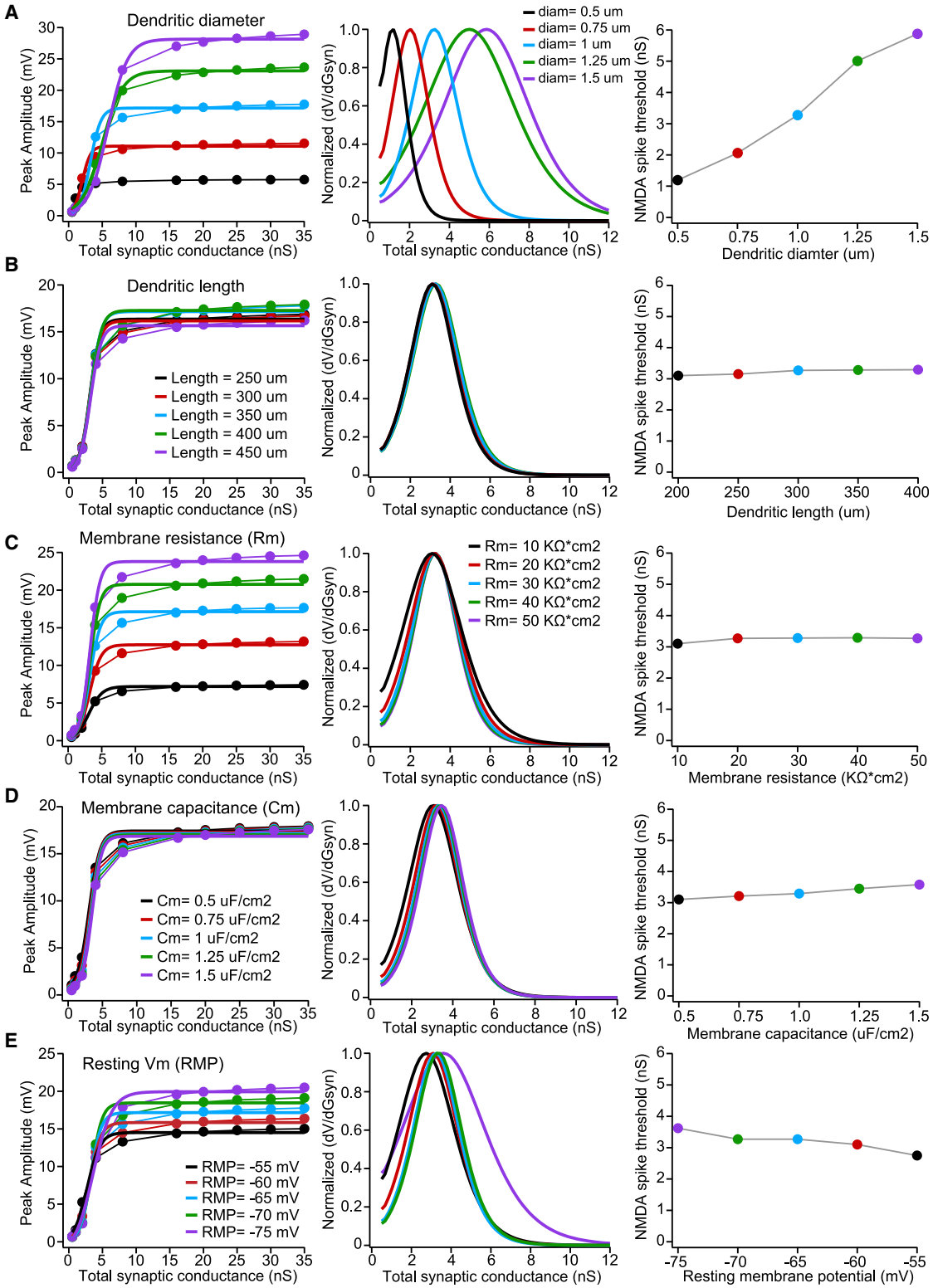

Figure 5. Impact of different passive and morphological parameters on NMDA spike generation in a simplified "ball and stick" model

Left: plots of the peak voltage response in the somatic compartment versus the total synaptic conductance for models with different dendritic diameter (A), dendritic length (B), specific membrane resistance (R_m; C), specific membrane capacitance (C_m; D), and resting membrane potential (V_m; E). All data are fitted with

(legend continued on next page)

(Figure 3B), essentially doubled the synaptic threshold for NMDA spike generation in the ball and stick model (Figure 5A). These simulations indicate that the 2-fold difference in NMDA spike threshold in the human and mouse L2/3 models (Figure 3F) is primarily due to the difference in basal dendrite diameter. Furthermore, they suggest that the reduced capacity of human neurons to generate NMDA spikes is likely to be a direct result of the wider diameter of human dendrites. Perhaps surprisingly, the reduced capacity of human dendrites to generate NMDA spikes was not compensated for by the larger size and higher density of spines in human neurons[33,34] nor by recent work indicating that human synapses are stronger and more reliable than those in mice.[27,32]

Consistent with our findings, recent work by Beaulieu-Laroche and colleagues[15] concluded that the more compartmentalized nature of human compared with rodent cortical L5 apical dendrites was in part due to their increased length. Other work on human neurons by Gidon and colleagues[14] found that AP backpropagation into the apical dendrites of human cortical L2/3 pyramidal neurons was weaker than in rodent L2/3 neurons, with apical dendritic spikes briefer and graded in amplitude. Together with our findings, these observations suggest that the active properties of human dendrites are different from those in rodents. In contrast, recent work in the apical dendrites of human L2/3 pyramidal neurons suggests that they are similar to their rodent counterparts.[17] Clearly, more work needs to be done to determine how human dendrites integrate the synaptic inputs they receive and how this compares with what is already known about dendritic integration in other species.

Limitations of the study

The most significant limitation of our study is that we cannot rule out that factors such as differences in tissue quality, the long-term impact of medication, or the older age of human compared with mouse tissue impacted on the conclusions from our study. That our experimental observations were reproduced in morphologically realistic models suggests this was not the case.

STAR★METHODS

Detailed methods are provided in the online version of this paper and include the following:

SUPPLEMENTAL INFORMATION

Supplemental information can be found online at https://doi.org/10.1016/j.celrep.2022.111787.

ACKNOWLEDGMENTS

This research was funded by an Australian Research Council Discovery Project grant to G.J.S. and L.M.P. (DP190103296) and the Sylvia and Charles Viertel Charitable Foundation (L.M.P.).

AUTHOR CONTRIBUTIONS

G.J.S., L.M.P., and G.T.-S. initiated and designed the project. G.T.-S., M.R., S.H., A.M.M., and R.G. acquired and analyzed the experimental data. J.K. and K.D. obtained the human tissue. C.F. coordinated tissue collection. S.H. performed analysis and all computational modeling. G.J.S. and L.M.P. supervised the project. G.J.S. and S.H. prepared the figures, and G.J.S., L.M.P., M.R., G.T.-S., S.H., and R.G. wrote the paper, which was edited by all authors.

DECLARATION OF INTERESTS

The authors declare no competing interests.

Received: March 25, 2022
Revised: August 19, 2022
Accepted: November 15, 2022
Published: December 13, 2022

REFERENCES

1. Stuart, G.J., and Spruston, N. (2015). Dendritic integration: 60 years of progress. Nat. Neurosci. *18*, 1713–1721. https://doi.org/10.1038/nn.4157.
2. Johnston, D., Magee, J.C., Colbert, C.M., and Cristie, B.R. (1996). Active properties of neuronal dendrites. Annu. Rev. Neurosci. *19*, 165–186. https://doi.org/10.1146/annurev.ne.19.030196.001121.
3. London, M., and Häusser, M. (2005). Dendritic computation. Annu. Rev. Neurosci. *28*, 503–532. https://doi.org/10.1146/annurev.neuro.28.061604.135703.
4. Sjöström, P.J., Rancz, E.A., Roth, A., and Häusser, M. (2008). Dendritic excitability and synaptic plasticity. Physiol. Rev. *88*, 769–840. https://doi.org/10.1152/physrev.00016.2007.
5. Magee, J.C., and Grienberger, C. (2020). Synaptic plasticity forms and functions. Annu. Rev. Neurosci. *43*, 95–117. https://doi.org/10.1146/annurev-neuro-090919-022842.
6. Palmer, L.M., Shai, A.S., Reeve, J.E., Anderson, H.L., Paulsen, O., and Larkum, M.E. (2014). NMDA spikes enhance action potential generation during sensory input. Nat. Neurosci. *17*, 383–390. https://doi.org/10.1038/nn.3646.
7. Larkum, M.E., Nevian, T., Sandler, M., Polsky, A., and Schiller, J. (2009). Synaptic integration in tuft dendrites of layer 5 pyramidal neurons: a new unifying principle. Science *325*, 756–760. https://doi.org/10.1126/science.1171958.

sigmoids. Middle: plots of differentiated and normalized sigmoid fits versus the total synaptic conductance for models with different dendritic diameter (A), dendritic length (B), R_m (C), C_m (D), and resting membrane potential (E). Right: plots of NMDA spike threshold versus dendritic diameter (A), dendritic length (B), R_m (C), C_m (D), and resting membrane potential (E). NMDA spike threshold was defined as the synaptic conductance at the peak of differentiated sigmoid fits (middle). Data are color coded as indicated in the legends.

8. Takahashi, N., Oertner, T.G., Hegemann, P., and Larkum, M.E. (2016). Active cortical dendrites modulate perception. Science *354*, 1587–1590. https://doi.org/10.1126/science.aah6066.

9. Lavzin, M., Rapoport, S., Polsky, A., Garion, L., and Schiller, J. (2012). Nonlinear dendritic processing determines angular tuning of barrel cortex neurons in vivo. Nature *490*, 397–401. https://doi.org/10.1038/nature11451.

10. Smith, S.L., Smith, I.T., Branco, T., and Häusser, M. (2013). Dendritic spikes enhance stimulus selectivity in cortical neurons in vivo. Nature *503*, 115–120. https://doi.org/10.1038/nature12600.

11. Xu, N.L., Harnett, M.T., Williams, S.R., Huber, D., O'Connor, D.H., Svoboda, K., and Magee, J.C. (2012). Nonlinear dendritic integration of sensory and motor input during an active sensing task. Nature *492*, 247–251. https://doi.org/10.1038/nature11601.

12. Bittner, K.C., Milstein, A.D., Grienberger, C., Romani, S., and Magee, J.C. (2017). Behavioral time scale synaptic plasticity underlies CA1 place fields. Science *357*, 1033–1036. https://doi.org/10.1126/science.aan3846.

13. Cichon, J., and Gan, W.B. (2015). Branch-specific dendritic Ca spikes cause persistent synaptic plasticity. Nature *520*, 180–185. https://doi.org/10.1038/nature14251.

14. Gidon, A., Zolnik, T.A., Fidzinski, P., Bolduan, F., Papoutsi, A., Poirazi, P., Holtkamp, M., Vida, I., and Larkum, M.E. (2020). Dendritic action potentials and computation in human layer 2/3 cortical neurons. Science *367*, 83–87. https://doi.org/10.1126/science.aax6239.

15. Beaulieu-Laroche, L., Toloza, E.H.S., van der Goes, M.S., Lafourcade, M., Barnagian, D., Williams, Z.M., Eskandar, E.N., Frosch, M.P., Cash, S.S., and Harnett, M.T. (2018). Enhanced dendritic compartmentalization in human cortical neurons. Cell *175*, 643–651.e14. https://doi.org/10.1016/j.cell.2018.08.045.

16. Beaulieu-Laroche, L., Brown, N.J., Hansen, M., Toloza, E.H.S., Sharma, J., Williams, Z.M., Frosch, M.P., Cosgrove, G.R., Cash, S.S., and Harnett, M.T. (2021). Allometric rules for mammalian cortical layer 5 neuron biophysics. Nature *600*, 274–278. https://doi.org/10.1038/s41586-021-04072-3.

17. Gooch, H.M., Bluett, T., Perumal, M.B., Vo, H.D., Fletcher, L.N., Papacostas, J., Jeffree, R.L., Wood, M., Colditz, M.J., McMillen, J., et al. (2022). High-fidelity dendritic sodium spike generation in human layer 2/3 neocortical pyramidal neurons. Cell Rep. *41*, 111500. https://doi.org/10.1016/j.celrep.2022.111500.

18. Kalmbach, B.E., Hodge, R.D., Jorstad, N.L., Owen, S., de Frates, R., Yanny, A.M., Dalley, R., Mallory, M., Graybuck, L.T., Radaelli, C., et al. (2021). Signature morpho-electric, transcriptomic, and dendritic properties of human layer 5 neocortical pyramidal neurons. Neuron *109*, 2914–2927.e5, e2915. https://doi.org/10.1016/j.neuron.2021.08.030.

19. Nevian, T., Larkum, M.E., Polsky, A., and Schiller, J. (2007). Properties of basal dendrites of layer 5 pyramidal neurons: a direct patch-clamp recording study. Nat. Neurosci. *10*, 206–214. https://doi.org/10.1038/nn1826.

20. Schiller, J., Major, G., Koester, H.J., and Schiller, Y. (2000). NMDA spikes in basal dendrites of cortical pyramidal neurons. Nature *404*, 285–289. https://doi.org/10.1038/35005094.

21. Polsky, A., Mel, B.W., and Schiller, J. (2004). Computational subunits in thin dendrites of pyramidal cells. Nat. Neurosci. *7*, 621–627. https://doi.org/10.1038/nn1253.

22. Branco, T., and Häusser, M. (2011). Synaptic integration gradients in single cortical pyramidal cell dendrites. Neuron *69*, 885–892. https://doi.org/10.1016/j.neuron.2011.02.006.

23. Fletcher, L.N., and Williams, S.R. (2019). Neocortical topology governs the dendritic integrative capacity of layer 5 pyramidal neurons. Neuron *101*, 76–90.e4. https://doi.org/10.1016/j.neuron.2018.10.048.

24. Vetter, P., Roth, A., and Häusser, M. (2001). Propagation of action potentials in dendrites depends on dendritic morphology. J. Neurophysiol. *85*, 926–937. https://doi.org/10.1152/jn.2001.85.2.926.

25. Kalmbach, B.E., Buchin, A., Long, B., Close, J., Nandi, A., Miller, J.A., Bakken, T.E., Hodge, R.D., Chong, P., de Frates, R., et al. (2018). H-channels contribute to divergent intrinsic membrane properties of supragranular pyramidal neurons in human versus mouse cerebral cortex. Neuron *100*, 1194–1208.e5. https://doi.org/10.1016/j.neuron.2018.10.012.

26. Bock, T., and Stuart, G.J. (2016). Impact of calcium-activated potassium channels on NMDA spikes in cortical layer 5 pyramidal neurons. J. Neurophysiol. *115*, 1740–1748. https://doi.org/10.1152/jn.01047.2015.

27. Eyal, G., Verhoog, M.B., Testa-Silva, G., Deitcher, Y., Benavides-Piccione, R., DeFelipe, J., de Kock, C.P.J., Mansvelder, H.D., and Segev, I. (2018). Human cortical pyramidal neurons: from spines to spikes via models. Front. Cell. Neurosci. *12*, 181. https://doi.org/10.3389/fncel.2018.00181.

28. Mohan, H., et al. (2015). Dendritic and axonal architecture of individual pyramidal neurons across layers of adult human neocortex. Cereb Cortex *25*, 4839–4853. https://doi.org/10.1093/cercor/bhv188.

29. Behabadi, B.F., Polsky, A., Jadi, M., Schiller, J., and Mel, B.W. (2012). Location-dependent excitatory synaptic interactions in pyramidal neuron dendrites. PLoS Comput. Biol. *8*, e1002599. https://doi.org/10.1371/journal.pcbi.1002599.

30. Major, G., Polsky, A., Denk, W., Schiller, J., and Tank, D.W. (2008). Spatiotemporally graded NMDA spike/plateau potentials in basal dendrites of neocortical pyramidal neurons. J. Neurophysiol. *99*, 2584–2601. https://doi.org/10.1152/jn.00011.2008.

31. Branco, T., Clark, B.A., and Häusser, M. (2010). Dendritic discrimination of temporal input sequences in cortical neurons. Science *329*, 1671–1675. https://doi.org/10.1126/science.1189664.

32. Hunt, S., et al. (2022). Strong and reliable synaptic communication between pyramidal neurons in adult human cerebral cortex. Cereb Cortex. https://doi.org/10.1093/cercor/bhac246.

33. Benavides-Piccione, R., Ballesteros-Yáñez, I., DeFelipe, J., and Yuste, R. (2002). Cortical area and species differences in dendritic spine morphology. J. Neurocytol. *31*, 337–346. https://doi.org/10.1023/a:1024134312173.

34. DeFelipe, J., Alonso-Nanclares, L., and Arellano, J.I. (2002). Microstructure of the neocortex: comparative aspects. J. Neurocytol. *31*, 299–316. https://doi.org/10.1023/a:1024130211265.

35. Carnevale, N.T., and Hines, M.L. (2006). The Neuron Book (Cambridge Univ Press).

36. Ding, F., O'Donnell, J., Xu, Q., Kang, N., Goldman, N., and Nedergaard, M. (2016). Changes in the composition of brain interstitial ions control the sleep-wake cycle. Science *352*, 550–555. https://doi.org/10.1126/science.aad4821.

37. Sanchez-Vives, M.V., and McCormick, D.A. (2000). Cellular and network mechanisms of rhythmic recurrent activity in neocortex. Nat. Neurosci. *3*, 1027–1034. https://doi.org/10.1038/79848.

38. Eyal, G., Verhoog, M.B., Testa-Silva, G., Deitcher, Y., Lodder, J.C., Benavides-Piccione, R., Morales, J., DeFelipe, J., de Kock, C.P., Mansvelder, H.D., and Segev, I. (2016). Unique membrane properties and enhanced signal processing in human neocortical neurons. Elife *5*, e16553. https://doi.org/10.7554/eLife.16553.

39. Bekkers, J.M., Richerson, G.B., and Stevens, C.F. (1990). Origin of variability in quantal size in cultured hippocampal neurons and hippocampal slices. ProcProc. Natl. Acad. Sci. USA *87*, 5359–5362. https://doi.org/10.1073/pnas.87.14.5359.

40. Manabe, T., Renner, P., and Nicoll, R.A. (1992). Postsynaptic contribution to long-term potentiation revealed by the analysis of miniature synaptic currents. Nature *355*, 50–55. https://doi.org/10.1038/355050a0.

41. Gil, Z., and Amitai, Y. (2000). Evidence for proportional synaptic scaling in neocortex of intact animals. Neuroreport *11*, 4027–4031. https://doi.org/10.1097/00001756-200012180-00025.

42. Myme, C.I.O., Sugino, K., Turrigiano, G.G., and Nelson, S.B. (2003). The NMDA-to-AMPA ratio at synapses onto layer 2/3 pyramidal neurons is conserved across prefrontal and visual cortices. J. Neurophysiol. *90*, 771–779. https://doi.org/10.1152/jn.00070.2003.

43. Jahr, C.E., and Stevens, C.F. (1990). Voltage dependence of NMDA-activated macroscopic conductances predicted by single-channel kinetics. J. Neurosci. *10*, 3178–3182.

44. Rhodes, P. (2006). The properties and implications of NMDA spikes in neocortical pyramidal cells. J. Neurosci. *26*, 6704–6715. https://doi.org/10.1523/JNEUROSCI.3791-05.2006.

STAR★METHODS

KEY RESOURCES TABLE

REAGENT or RESOURCE	SOURCE	IDENTIFIER
Chemicals, peptides, and recombinant proteins		
Alexa 594	Thermo Fisher Scientific	Cat. # A10438
TMR biocytin	Thermo Fisher Scientific	Cat. # T12921
L-Glutamic acid	Tocris, UK	Cat. # 0218
D-(-)-2-Amino-5-phosphonopentanoic acid (APV)	Tocris, UK	Cat. # 0106
Experimental models: Organisms/strains		
C57/B6 mice	Charles River	C57BL/6NCrlAnu
Human brain tissue	Brain tumor or epilepsy patients	See Table S1
Software and algorithms		
NEURON simulation environment	Carnevale and Hines[35]	https://neuron.yale.edu/neuron/
NEURON simulation code for all models	Suraj Honnuraiah	https://github.com/gtsilva/Human_NMDA_Spikes

RESOURCE AVAILABILITY

Lead contact

Further information and requests for resources and reagents should be directed to and will be fulfilled by the lead contact, Greg Stuart (greg.stuart@anu.edu.au).

Materials availability

This study did not generate new unique reagents.

Data and code availability

- All data reported in this paper will be shared by the lead contact upon request.
- All original code has been deposited at Github and is publicly available as of the date of publication. DOIs are listed in the key resources table (https://github.com/gtsilva/Human_NMDA_Spikes).
- Any additional information required to reanalyze the data reported in this paper is available from the lead contact upon request.

EXPERIMENTAL MODEL AND SUBJECT DETAILS

Human brain tissue excess to that required for histopathology or removed incidentally for surgical access was obtained from patients undergoing neurosurgery to remove brain tumors or treat epilepsy (Table S1; performed by KD and JK, respectively). Written informed consent was obtained from patients (aged 18 to 70 years old) and all procedures were performed with the approval of the Human Research Ethical Committee (HREC) of the Royal Melbourne Hospital (HREC No: 2001:85 and 2020:214). The tissue obtained was from the anterior medial temporal cortex, the frontal cortex and the parieto-occipital cortex. After resection, tissue was placed immediately (<30s) in a cold and recently carbogenated solution containing (in mM): 125 NaCl, 25 $NaHCO_3$, 5 HEPES, 1 $CaCl_2$, 6 $MgCl_2$, 3 KCl, 1.25 NaH_2PO_4 and 10 Glucose. Samples were transported on ice until the slicing procedure, which occurred generally less than 15 min after resection. Rodent tissue was obtained from 6-8 week-old male or female mice. Mice were anesthetised by inhalation of isoflurane (3%) and decapitated prior to the brain being removed according to procedures approved by the Animal Ethics Committee of the Australian National University.

METHOD DETAILS

Slice preparation

Brain tissue was sliced using a vibrating tissue slicer (Leica Microsystems) in ice-cold carbogenated solution containing (in mM): 110 Choline Chloride, 26 $NaHCO_3$, 11.6 Na-Ascorbate, 7 $MgCl_2$, 3.1 Na-pyruvate, 2.5 KCl, 1.25 NaH_2PO_4, 0.5 $CaCl_2$ and 10 Glucose. Coronal tissue slices (300–400 μm thick) were obtained containing temporal, frontal or parieto-occipital cortex. Slices were incubated in carbogenated solution containing (in mM): 125 NaCl, 25 $NaHCO_3$, 5 HEPES, 1 $CaCl_2$, 6 $MgCl_2$, 3 KCl, 1.25 NaH_2PO_4 and 10 Glucose at 35°C for 30 min and thereafter at room temperature until required. Recordings were performed in artificial cerebrospinal

fluid (ACSF) with composition (in mM): 125 NaCl, 25 $NaHCO_3$, 3 KCl, 1.2 $CaCl_2$, 0.7 $MgCl_2$, 1.25 mM NaH2PO4 and 10 Glucose. These ionic concentrations are similar to those found in cerebrospinal fluid.[36,37]

Electrophysiology

Whole-cell patch-clamp recordings were made from the soma of L2/3 pyramidal neurons using an Olympus BX51 WI microscope equipped with a fluorescent imaging system. Slices were continuously perfused with carbogenated ACSF at a rate of 2mL/min at 34°C (±1°C). Borosilicate glass pipettes (inner diameter 0.86 mm, outer diameter 1.5 mm, Sutter) were pulled using an electrode puller (Sutter Instruments, USA) and had open tip resistances of 4–6 MΩ. Recording pipettes were filled with intracellular solution of the following composition (in mM): 130 K-Gluconate, 10 KCl, 10 HEPES, 4 Mg^{2+}-ATP, 0.3 Na_2-GTP, 10 Na_2-Phosphocreatine (pH set to 7.25 with KOH, osmolarity 285 mosmol/L). 5 μM of the fluorescent dye Alexa 594 or 0.02% TMR biocytin (Thermo Fisher Scientific) was included in the intracellular solution to visualise basal and oblique dendrites. Current clamp recordings were made using a current-clamp amplifier (BVC-700A; Dagan Corp., Minneapolis, MN or Multiclamp 700B; Molecular Devices, San Jose, USA) mounted on a remotely controlled micromanipulators (Luigs and Neumann, Germany). Cells were excluded from data analysis if the somatic resting membrane potential was more depolarised than −55 mV or if fluctuations in membrane potential >5 mV were observed at any time during the recording. Cells were also excluded if the somatic series resistance exceeded 50 MΩ or if the somatic series resistance changed by more than 10% during the recording. Membrane potential was not corrected for liquid junction potentials.

Electrophysiological data were filtered at 10 kHz and acquired at 50 kHz by a Macintosh computer running Axograph X acquisition software (Axograph Scientific, Sydney, Australia) using an ITC-18 interface (Instrutech/HEKA, Germany), or by a Windows computer running Clampex 10.7 (Molecular Devices) using a Digidata 1440A interface (Molecular Devices, San Jose, USA).

Glutamate iontophoresis

L-Glutamic acid (Tocris, UK) was dissolved in ACSF to a concentration of 200 mM and the pH adjusted to 7.4 with NaOH. 1 μM of the fluorescent dye Alexa 594 was added to the glutamate solution to help visualise the pipette tip under fluorescent light. Iontophoretic pipettes were made from borosilicate glass (outer diameter of 1 mm; inner diameter of 0.5 mm) and pulled to give a tip resistance of 120-140 MΩ when filled. The iontophoretic pipette was connected to the 1x gain headstage of an Axoclamp 2A current/voltage-clamp amplifier (Molecular Devices, Sunnyvale, CA). A backing current of +5 nA was used to prevent spillage of glutamate from the iontophoretic pipette. The pipette was inserted into the slice and positioned under visual control in close proximity (within 5 μm) of a basal or oblique dendrite of the patched neuron at a location at least 120 μm from the soma (average ∼150 μm from the soma). Fluorescence was visualised using a CCD camera (CoolSNAP EZ, Photometrics, Tucson, AZ). Glutamate were applied using 20 to 30 ms negative current steps of varying amplitude before (control) and after application of D-(−)-2-Amino-5-phosphono-pentanoic acid (APV; 50 μM).

Extracellular stimulation

Extracellular stimulation pipettes were pulled from theta glass (outer diameter 1.5 mm, Sutter) to approximate tip diameters of 1–2 μm. Both barrels were filled with carbogenated ACSF containing 5 μM of the fluorescent dye Alexa 594 and connected to the positive and negative poles of an isolated stimulator (WPI, Getting Instruments or ISO-Flex). The pipette tip was positioned under visual control in close proximity (within 5 μm) of a basal dendrite of the patched neuron at a location at least 120 μm from the soma (average ∼150 μm from the soma). Brief (0.2 ms) pulses of different amplitude were used to evoke synaptic responses before (control) and after APV (50 μM).

Modeling

Computer simulations were performed using the NEURON 7.4 simulation environment.[35] The morphology of the human neuron was obtained from Eyal et al.,[27] whereas the mouse L2/3 pyramidal neuron was obtained from Smith et al.[10] While it has been suggested that C_m is lower in human compared to rodent neurons,[38] more recent work indicates this is unlikely to be the case.[15,17] As a result, we set C_m to 1 μF/cm^2 in both the human and mouse models and internal resistance (R_i) to 150 Ω.cm. To match the experimentally observed human and mouse somatic input resistances (Figure S1), we set R_m to 10 kΩ.cm^2 in the human and 40 kΩ.cm^2 in the mouse L2/3 pyramidal neuron model, giving somatic input resistances of approximately 40 MΩ and 100 MΩ, respectively. These values are similar to that observed experimentally (human L2/3 neurons: 35.9 ± 2.3 MΩ, n = 39; mouse L2/3 neurons: 88.36 ± 2.64 MΩ; n = 59). The resting membrane potential was set to −65 mV in the human and −75 mV in the mouse L2/3 pyramidal neuron model to match the experimentally observed values (Figure S1). These values are similar to that observed experimentally (human L2/3 neurons: −67.7 ± 0.5 mV, n = 39; mouse L2/3 neurons: −75.4 ± 0.9 mV, n = 59). Dendritic compartments were not adjusted for spines and did not contain voltage-activated channels. Different numbers of synaptic inputs containing both AMPA (250 pS) and NMDA (500 pS) components were randomly placed on basal dendrites within a restricted dendritic region (10 um in length) with its center ∼150 μm from the soma. Unitary (single synapse) AMPA conductances have been estimated to be between 50 and 210 pS.[39,40] Given space clamp issues with these measurements a unitary AMPA conductance of 250 pS is realistic. Other work indicates that the NMDA conductance is between 110 and ∼770% of the AMPA conductance, based on data from evoked EPSCs in cortical layer 2/3 neurons.[41,42] Using an NMDA/AMPA conductance ratio of 2 as the default in our simulations is within this range and similar

to that used by other simulation studies.[7] The rise time of the AMPA and NMDA conductance was set to 0.3 ms and 30 ms, respectively, whereas the decay time constant was set to 5 ms and 200 ms, respectively (Spruston et al., 1995, Hausser et al., 1997, Larkum et al. 2009). The default Mg^{2+} block of the NMDA conductance (g_{NMDA}) was modeled using the equation: $g_{NMDA} = 1/[1 + \exp(-0.08 *V) * (0.7/3.57)]$, based on the formalism from Jahr and Stevens 1990 [43], but with the default NMDA slope factor changed from 0.062 to 0.08 [44] and the default external magnesium concentration set to 0.7 mM, as used in experiments.

In the simplified "ball and stick" model, a somatic compartment (dimensions: 90 μm by 90 μm) was connected to a single dendritic compartment with default dimension of 300 μm length and 1 μm width. The default passive properties were R_m = 30 kΩ.cm^2, C_m = 1 μF/cm^2 and R_i = 150 Ω.cm. The default resting membrane potential was set to −65 mV. A single synaptic input of varying magnitude with a default AMPA to NMDA conductance ratio of 2 was placed in the dendritic compartment 150 μm from the somatic compartment. In different simulations the dimensions of the dendritic compartment, R_m and C_m, the resting membrane potential, the NMDA/AMPA conductance ratio, and the NMDA slope factor and external magnesium concentration, were systematically varied to investigate their impact on the magnitude of the synaptic conductance required to generate an NMDA spike. All simulations used an integration time constant of 25 μs.

QUANTIFICATION AND STATISTICAL ANALYSIS

Data analysis was performed using Axograph X in combination with IGOR Pro or using Clampfit 10.7. GraphPad Prism was used for statistical analysis. Pooled data are presented as mean ± standard error of the mean (SEM). Plots of EPSP/NMDA spike amplitude versus iontophoretic current or extracellular stimulation intensity in control were fitted with a sigmoidal relationship, whereas data in the presence of APV was fitted with a line. For sigmoidal fitting the baseline was set at zero. The maximum slope of the sigmoid in control was determined by differentiating the sigmoidal fit and finding its peak. For each cell we then plotted the maximum slope of the sigmoid in control or the slope of the linear fit in APV versus the maximum voltage obtained during the highest iontophoretic current or extracellular stimulation intensity used (see plots in Figures 1D, Figures 2E and 2F). Plots of EPSP amplitude versus the number of synapses or synaptic conductance in the different models were also fitted with a sigmoidal relationship. The baseline was set at zero for all sigmoidal fits. The peak of differentiated sigmoidal fits, which occurs at the sigmoid midpoint, was used to determine the "threshold" number of synaptic inputs or synaptic conductance required to evoke an NMDA spike in the models.

Analysis of the AMP and NMDA component of EPSPs was performed on EPSPs evoked by extracellular stimulation at the lowest intensity tested. That is, at a stimulation intensity well below NMDA spike threshold. The NMDA component of EPSPs in difference human and mouse neurons was determined by subtraction of the EPSP in APV from that in control, whereas the AMPA component of EPSPs was determined from the EPSP in APV.